HIGH POWER LASER
SCIENCE AND ENGINEERING

RESEARCH ARTICLE

Effect of subsurface impurity defects on laser damage resistance of beam splitter coatings

Wenyun Du[1,2], Meiping Zhu[1,2,3,4], Jun Shi[1,2,3], Tianbao Liu[1,2], Jian Sun[1], Kui Yi[1], and Jianda Shao[1,2,3,4]

[1] *Laboratory of Thin Film Optics, Key Laboratory of Materials for High Power Laser, Shanghai Institute of Optics and Fine Mechanics, Chinese Academy of Sciences, Shanghai, China*

[2] *Center of Materials Science and Optoelectronics Engineering, University of Chinese Academy of Sciences, Beijing, China*

[3] *Hangzhou Institute for Advanced Study, University of Chinese Academy of Sciences, Hangzhou, China*

[4] *CAS Center for Excellence in Ultra-intense Laser Science, Shanghai, China*

Abstract

The laser-induced damage threshold (LIDT) of plate laser beam splitter (PLBS) coatings is closely related to the subsurface absorption defects of the substrate. Herein, a two-step deposition temperature method is proposed to understand the effect of substrate subsurface impurity defects on the LIDT of PLBS coatings. Firstly, BK7 substrates are heat-treated at three different temperatures. The surface morphology and subsurface impurity defect distribution of the substrate before and after the heat treatment are compared. Then, a PLBS coating consisting of alternating HfO_2–Al_2O_3 mixture and SiO_2 layers is designed to achieve a beam-splitting ratio (transmittance to reflectance, s-polarized light) of approximately 50:50 at 1053 nm and an angle of incidence of 45°, and it is prepared under four different deposition processes. The experimental and simulation results show that the subsurface impurity defects of the substrate migrate to the surface and accumulate on the surface during the heat treatment, and become absorption defect sources or nodule defect seeds in the coating, reducing the LIDT of the coating. The higher the heat treatment temperature, the more evident the migration and accumulation of impurity defects. A lower deposition temperature (at which the coating can be fully oxidized) helps to improve the LIDT of the PLBS coating. When the deposition temperature is 140°C, the LIDT (s-polarized light, wavelength: 1064 nm, pulse width: 9 ns, incident angle: 45°) of the PLBS coating is 26.2 J/cm², which is approximately 6.7 times that of the PLBS coating deposited at 200°C. We believe that the investigation into the laser damage mechanism of PLBS coatings will help to improve the LIDT of coatings with partial or high transmittance at laser wavelengths.

Keywords: laser-induced damage threshold; nodule defect; plate laser beam splitter; subsurface impurity defect

1. Introduction

Laser coating is a key component of high-power laser systems, such as inertial confinement fusion[1–3], and its laser-induced damage threshold (LIDT) directly affects the output power of high-power laser systems. Various defects in the coating and substrate can be sources of damage under laser irradiation. The effect of defects on the LIDT of coatings depends on the properties of the defects and coatings. For example, for coatings with partial or high transmittance at the laser wavelength (such as anti-reflection coatings, beam splitter coatings), the effect

of substrate subsurface impurities on the LIDT is much greater than that of coatings with high reflectance at the laser wavelength[4,5]. Subsurface defects are generated during the chemical–mechanical polishing of substrates. Subsurface damage layers generally consist of a re-deposition layer (also known as the Beilby layer), a defect layer containing cracks and scratches and a deformed layer. Impurity particles are randomly distributed in the re-deposition layer, some of which are embedded in the scratches and cracks of the defect layer[6]. For a specified irradiated laser fluence, compared with a high-reflection coating, the laser intensity of a coating with partial or high transmittance is stronger at the substrate–coating interface, and subsurface impurity defects are more likely to cause damage under laser irradiation. In addition, the electron beam deposition process often requires the substrate to be heated, and subsurface impurities can easily

---

1

migrate to the surface during heating[7,8]. Researchers have simulated the effect of impurity particles on the LIDT of substrates using Mie scattering theory and impurity defect absorption models[9,10]. Several studies have been conducted to investigate the formation process of the re-deposition layer[11,12], and reduce subsurface impurities by improving the polishing process[13], using ion beam etching[14–16], using acid etching[15–17] and so on. However, the mechanism by which subsurface impurities affect the LIDT of coatings with partial or high transmittance at laser wavelengths, such as plate laser beam splitter (PLBS) coatings, remains to be investigated.

In this study, a two-step deposition temperature method is proposed to analyze the role of subsurface impurity defects in the laser-induced damage mechanism of PLBS coatings. Firstly, BK7 substrates are heat-treated at different temperatures, and the effects of the heat treatment temperature on the surface morphology and impurity element distribution of the substrate are investigated. Then, a PLBS coating is designed to achieve an s-polarized transmittance (T) of $50\% \pm 3\%$ at 1053 nm and an incident angle of 45°, and it is prepared using four different deposition processes. The optical, mechanical and LIDT properties of the four PLBS coatings are investigated. Finally, the laser-induced damage mechanism of the PLBS coating is simulated and analyzed using the finite-element method (FEM).

2. Materials and methods

2.1. Substrate heat treatment

The BK7 substrate is subjected to heat treatment at three different temperatures to simulate the heating process during the deposition of the coating and to investigate the thermal migration and aggregation of substrate subsurface impurities at different temperatures. Heat treatment is performed in a tubular furnace equipped with a quartz tube (Nabertherm, RS 80/300/11). Prior to the heat treatment, the samples are ultrasonically cleaned in deionized water and placed in a covered glass Petri dish for annealing to avoid contamination. The heat treatment process includes the following steps: firstly, the quartz tube is evacuated using a mechanical pump, and the vacuum degree is maintained at approximately 0.8 Pa. Then, the temperature inside the quartz tube is increased from room temperature to the set temperature at a rate of 2.2°C/min, and maintained at this temperature for 2 h. Finally, the quartz tube is naturally cooled to room temperature. The specific heat treatment temperatures of the blank substrates are listed in Table 1, and a blank substrate without heat treatment is used for comparison.

2.2. Coating preparation

A PLBS coating is designed to achieve a T of $50\% \pm 3\%$ at 1053 nm and an incident angle of 45°. The PLBS coating

Table 1. Detailed information of the blank substrates.

Sample number	Heat treatment temperature (°C)
HB1	/
HB2	100
HB3	140
HB4	200

structure is as follows: substrate|2LMLMLM2L|air. Here, M and L represent the HfO_2–Al_2O_3 mixture and SiO_2 layers with a quarter-wave optical thickness (QWOT) at a reference wavelength of 1180 nm, respectively. The numbers before M and L represent the optical thickness of the corresponding material in the units of the QWOT. The designed refractive indices of the M and L layers at 1180 nm are 1.414 and 1.669, respectively. The PLBS coatings are deposited via electron beam evaporation using four different deposition processes (A1, A2, A3 and B1). Except for the deposition temperature, all other deposition parameters are the same. PLBS coatings are deposited on BK7 ($\Phi50$ mm $\times$ 5 mm) and fused silica substrates, where the former is used for stress characterization and LIDT measurements, and the latter for other measurements. All the substrates are ultrasonically cleaned in deionized water before being loaded into the coating chamber, followed by plasma ion cleaning prior to deposition[18]. The coating chamber is heated to the set temperature and evacuated to a base pressure of 5×10^{-4} Pa. The deposition rates of Al_2O_3 and HfO_2 in the HfO_2–Al_2O_3 mixture layer and that of SiO_2 in the SiO_2 layer are 0.058, 0.024 and 0.200 nm/s, respectively. The oxygen pressures for the HfO_2–Al_2O_3 mixture and SiO_2 layers are 1.5×10^{-2} and 5.0×10^{-3} Pa, respectively. The interfaces between the alternating layers are all sandwich-like-structure interfaces; the sandwich-like-structure interfaces and the HfO_2–Al_2O_3 mixture layers are obtained via double electron beam co-evaporation[19,20]. The detailed deposition parameters are presented in Table 2. The layer adjacent to the substrate (layer 1) can be considered as two sublayers (sublayers 1 and 2). Different deposition temperatures are used for sublayers 1 and 2 in coatings A2 and A3, respectively. After sublayer 1 is deposited, the chamber is heated to 200°C and maintained at this temperature for 2 h before the remaining layers are deposited.

2.3. Sample characterization

The surface morphologies of the blank substrates are characterized using an atomic force microscope (AFM; Veeco Dimension 3100). For each sample, a 5 μm $\times$ 5 μm scan area is sampled in tapping mode, and detailed dimensional information regarding the particles on the surface of the sample is extracted using AFM software. The subsurface impurities of the substrates are investigated using time-of-flight secondary ion mass spectrometry (TOF-SIMS; ULVAC-PHI, PHI nano

Table 2. Detailed deposition temperatures of the four PLBS coatings.

| Layer | | Deposition temperature (°C) | | | | Physical thickness (nm) |
		A1	A2	A3	B1	
1	Sublayer 1	200	140	100	140	300.0
	Sublayer 2	200	200	200	140	114.8
	2–7	200	200	200	140	/

TOF III). The sputtering area is 400 μm × 400 μm, and the analysis area is 40 μm × 40 μm. The transmittance spectra of the coatings are measured using a spectrometer (Lambda 1050 UV/VIS/NIR, Perkin-Elmer), and the reflectance data are calculated from the transmittance data, neglecting the absorption. The microstructure of the coating is investigated via X-ray diffraction (XRD; PANalytical Empyrean) using Cu–Kα radiation in the 2θ range of 10°–90°. The sample surface is characterized using an interferometer (ZYGO Mark III-GPI) at 632.8 nm before (substrate) and 45 days after deposition (coating). All coatings are stored and characterized in a controlled environment at a temperature of 23°C ± 1.5°C and a relative humidity of 45% ± 5%. The stress of the coating is calculated using the Stoney's equation[21]. Typical O 1s spectra of the SiO_2 layer and the HfO_2–Al_2O_3 mixture layer are analyzed using X-ray photoelectron spectroscopy (XPS; Thermo Scientific) with a monochromatic Al Ka (1486.6 eV) X-ray source. The binding energy of the O element in the XPS spectra is calibrated using the C 1s peak (284.8 eV). The LIDT measurement is performed in the one-on-one test mode according to standard ISO 21254. A 1ω s-polarized neodymium-doped yttrium aluminum garnet (Nd:YAG) laser (1064 nm, 9 ns) is used as the laser source with an incident angle of 45°. The effective spot area on the coating surface is approximately 0.85 mm². Fifteen sites are irradiated for each laser fluence. Considering the inhomogeneity between samples, measurement uncertainty of the laser spot area and laser energy fluctuation, the total error of the LIDT measurement is about ±15%[22]. The surface and cross-sectional damage morphologies are characterized using a focused ion beam scanning electron microscope (FIB-SEM; Carl Zeiss AURIGA Cross Beam). Absorption at 1064 nm is measured using a home-built system based on the surface thermal lensing technique[23]. The electric-field (E-filed) intensity distribution of the PLBS coating and the E-field enhancement and temperature rise caused by defects under laser irradiation are analyzed via FEM simulations. All laser-induced temperature-rise simulations are performed using the same input laser parameters. The calculation area is set as a rectangular area centered on the defect, with a total length of approximately 260 μm. Compared with the size of the nanoscale impurity defects, the calculation area can reasonably simulate the damage formation mechanism and explain the experimental results.

3. Results and discussion

3.1. Surface morphology and impurity element distribution of non-heat-treated and heat-treated substrates

The surface morphology of the heat-treated substrates is characterized by AFM and compared with that of a non-heat-treated substrate. After the heat treatment, nanoscale particles are observed on the sample surface, and the particle density increases with the heat treatment temperature, as shown in Figure 1(a). The number of raised particles on the surface of the four samples is compared in Figure 1(b). The detailed dimensional information of the three particles on the surface of sample HB4 heat-treated at 200°C is shown in Figure 1(c). The lateral dimensions of the particles are hundreds of nanometers, and the height is only a few nanometers.

Metal abrasives and cerium-containing polishing fluids used for substrate grinding or polishing, as well as alumina suspensions for ultrasonic cleaning of substrates, may introduce impurity elements, such as Fe, Ce and Al[12,24,25]. The depth profiles of Al, Fe and Ce impurity elements in the four substrates are detected using TOF-SIMS, as shown in Figure 2. Prior to characterization, all sample surfaces are etched for 15 s to remove surface contamination. Overall, with the increase of etching time, the intensity of Al, Fe and Ce elements decreases rapidly. The peak intensity of the heat-treated substrate is lower than that of the non-heat-treated substrate. The characterization results of the impurity element distribution and surface morphology suggest that the impurity elements migrate to the substrate surface during heat treatment and accumulate on the substrate surface to form impurity particles. The higher the heat treatment temperature, the more evident the migration and aggregation of impurities.

3.2. Optical and microstructural properties of PLBS coatings

The transmittance spectra of the PLBS coatings deposited by the four process parameters are shown in Figure 3(a). The *T* values at 1053 nm of the four coatings satisfy the design target of 50% ± 3% at an angle of incidence of 45°. The measured XRD spectra of the four PLBS coatings are shown in Figure 3(b). Except for two broad peaks corresponding
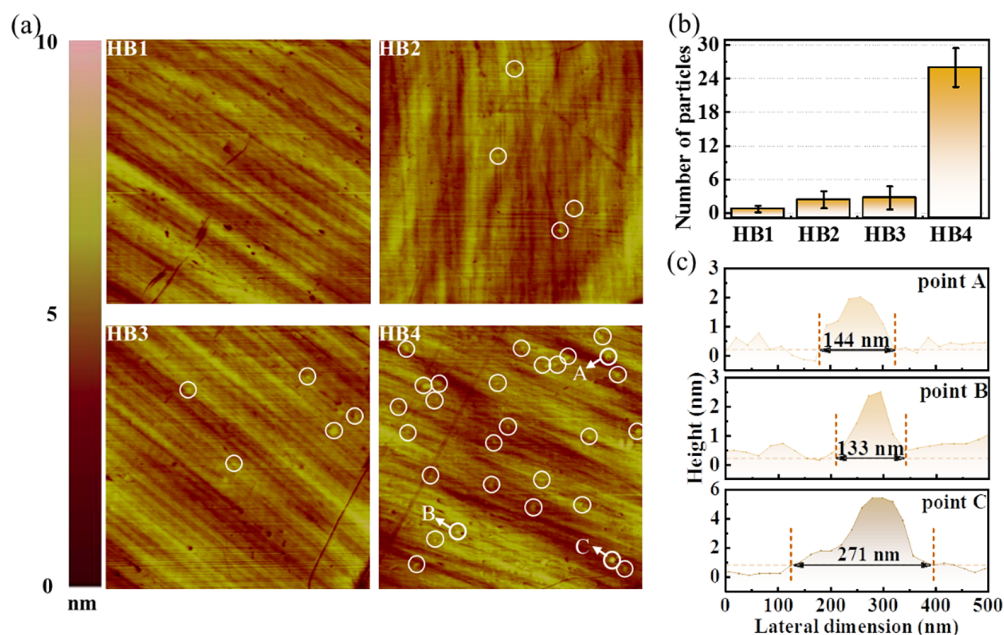
Figure 1. (a) Surface morphologies of a non-heat-treated substrate and substrates heat-treated at different temperatures. (b) The number of raised particles on the surface of the four samples. (c) Detailed dimensional information of particles at positions A, B and C on the surface of sample HB4.
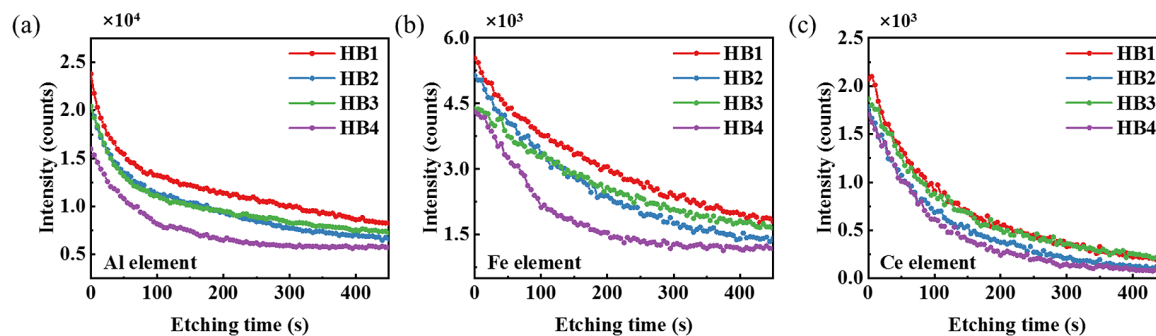

Figure 2. Depth profiles of (a) Al, (b) Fe and (c) Ce impurity elements characterized via TOF-SIMS.
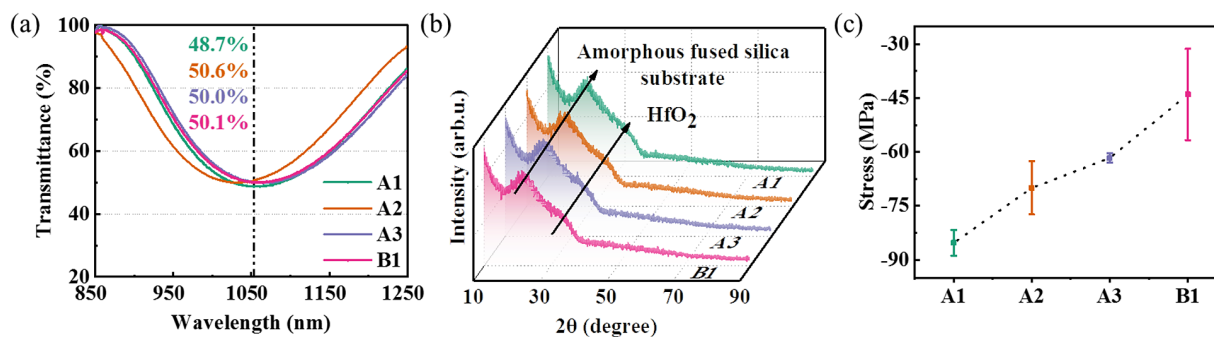

Figure 3. (a) Transmittance spectra, (b) measured XRD spectra and (c) coating stress measured after deposition (with an aging time of 45 days) of PLBS coatings.

to the fused silica substrate and HfO$_2$ phase, no other sharp peaks are observed, indicating that all HfO$_2$–Al$_2$O$_3$ mixture coatings are amorphous[26,27]. The coating stresses of the PLBS coatings measured after deposition (with an aging time of 45 days) are shown in Figure 3(c), and all coatings

exhibit compressive stress. The deposition temperature of sublayer 1 in coatings A1, A2 and A3 decreases gradually, and the measured compressive stress decreases accordingly. Compared with coating A2, coating B1 with sublayer 2 and layers 2–7 deposited at a lower temperature exhibits a
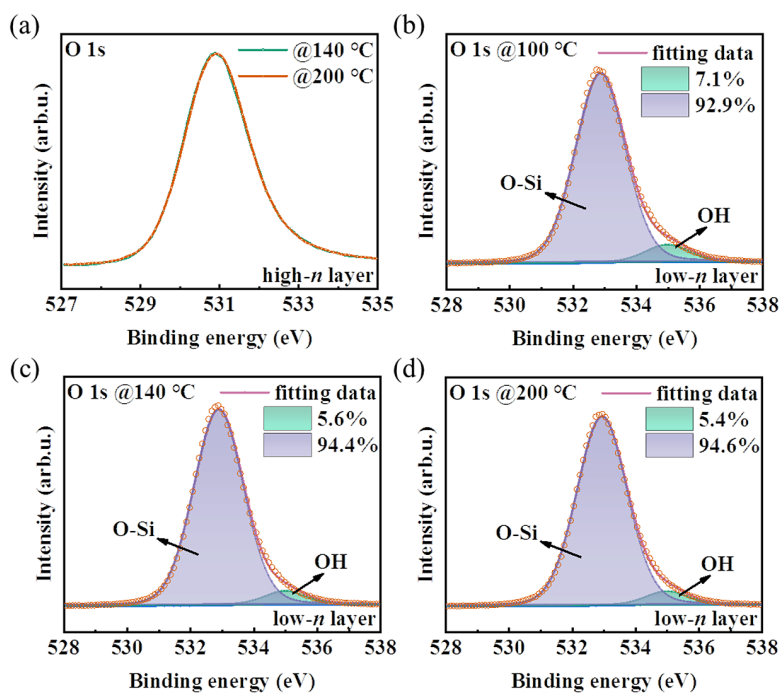
Figure 4. Typical O 1s spectra of (a) the high-*n* layer and low-*n* layers deposited at (b) 100°C, (c) 140°C and (d) 200°C.
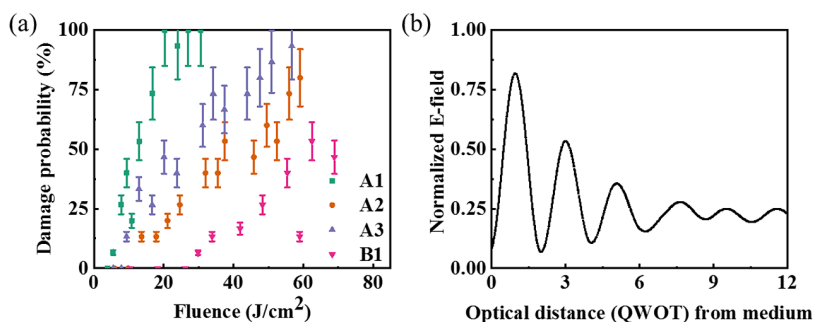

Figure 5. (a) Single-pulse damage probability as a function of the input fluence. (b) Normalized E-field intensity distribution in the PLBS coating.

lower compressive stress. These indicate that the lower the deposition temperature, the smaller the compressive stress of the PLBS coating.

XPS characterization is performed to investigate the stoichiometry of the HfO_2–Al_2O_3 mixture and the SiO_2 layers deposited at different temperatures. To characterize the HfO_2–Al_2O_3 mixture layer, layers 3–7 in coatings A1 and B1 are removed via 2 keV Ar^+ ion etching to expose the HfO_2–Al_2O_3 mixture layer before XPS scanning. To characterize the SiO_2 layer deposited at different temperatures, sublayer 2 in layer 1 and layers 2–7 in coatings A1, A2 and A3 are etched. Typical O 1s spectra of the HfO_2–Al_2O_3 mixture layers are shown in Figure 4(a). No significant difference is indicated in the O 1s spectra of the HfO_2–Al_2O_3 mixture layers deposited at 140°C and 200°C. Typical O 1s spectra of the SiO_2 layers deposited at different temperatures are shown in Figures 4(b)–4(d). All O 1s spectra can be fitted to two Lorentz–Gaussian peaks.

The peak at 532.9 eV corresponds to the O–Si bond, while the peak at 535.0 eV corresponds to the adsorbed OH bond caused by the adsorbed water in the coating[28]. The OH peak area ratio and the O/Si ratio (1.884 and 1.887 for 140°C and 200°C, respectively) of the SiO_2 layers deposited at 140°C and 200°C are close. While the deposition temperature of the SiO_2 layer decreases to 100°C, the OH peak area ratio increases and the O/Si ratio (1.864) decreases. The increase of sub-stoichiometry of the SiO_2 layer in coating A3 may lead to increased absorption of the coating, negatively affecting the LIDT of the coating[29].

3.3. LIDT and laser-induced damage mechanisms of PLBS coatings

A comparison of the laser-induced damage probabilities of the PLBS coatings deposited by the four processes is shown in Figure 5(a). The LIDTs of coatings A1, A2, A3 and B1 are
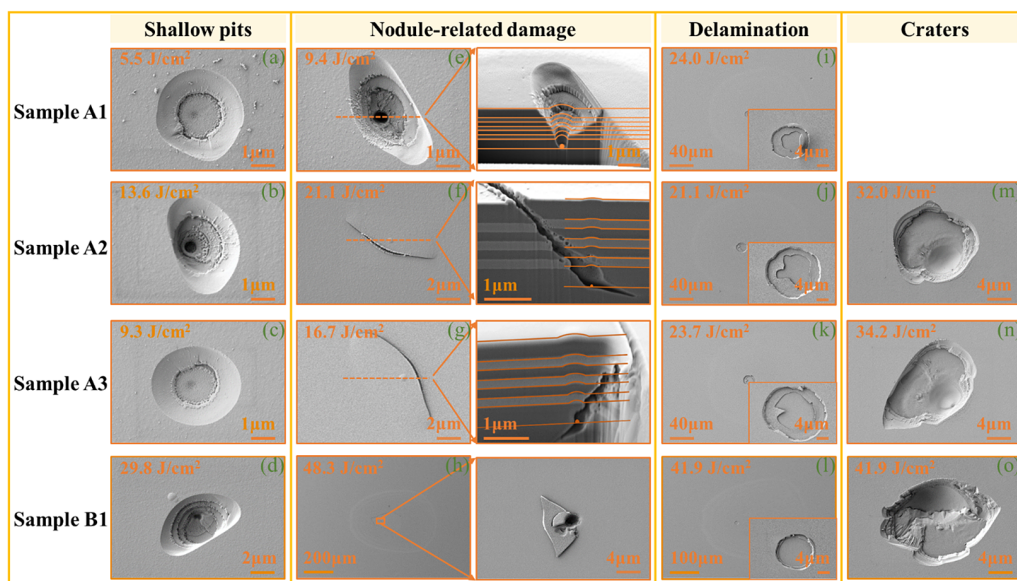
Figure 6. Typical damage morphologies of PLBS coatings.

determined to be 3.9, 9.8, 7.8 and 26.2 J/cm², respectively. Because the design structures of the four coatings are the same, the slight difference in *n* caused by the different deposition temperatures has no significant impact on the E-field distribution of the coatings. The normalized E-field distribution of the PLBS coating is shown in Figure 5(b). The peak intensity of the E-field decays from the air toward the substrate surface, but the E-field intensities at the substrate–coating interface and in the substrate are not zero. This indicates that the absorption defects at the substrate–coating interface or in the substrate may also absorb laser energy and induce damage under laser irradiation, thereby reducing the LIDT of the coating.

Typical damage morphologies are characterized using the FIB-SEM, and the four PLBS coatings exhibit similar damage morphologies. As shown in Figure 6, four typical morphological features are observed, namely shallow pits, nodule-related damage, delamination surrounded by plasma scalds and craters. The initial damage morphology is the shallow pit, and nanoscale pinpoints are observed in most of the shallow pits. The pinpoints are located at the layer–layer or substrate–coating interface. This suggests that the nanoscale defects at the interfaces are one of the main sources of laser-induced damage. Two nodule-related morphological features are observed with increasing input laser fluence. One morphological feature is the nodule-ejected pit, and the nodule geometry extracted from the cross-sectional image shown in Figure 6(e) indicates that the nodule seed is located on the substrate surface with a diameter of approximately 183 nm. The other morphological feature is a micro-crack surrounding a nodule, as shown in Figures 6(f) and 6(g), which is consistent with reports pertaining to un-ejected nodule damage[30]. The diameters of the nodule seeds in Figures 6(f) and 6(g) can be estimated using Equation (1)[31,32]:

$$D = \text{sqrt}\ (4dt), \qquad (1)$$

where *D* is the diameter of the nodule dome, *d* is the diameter of the nodule seed and *t* is the depth of the seed. The diameters of the nodule seeds in Figures 6(f) and 6(g) are approximately 31 and 62 nm, respectively. With a further increase in laser fluence, a delamination damage morphology surrounded by the plasma scald is observed. At a higher input laser fluence, crater-type damage morphology deep into the substrate can be observed. A pinpoint located in the substrate is observed in most craters, suggesting that this damage may be related to subsurface impurity defects[7]. No crater-type damage morphology is observed on coating A1 at the test laser fluence, since the maximum laser fluence used in the LIDT test is much lower than that used in other coating tests.

Figure 7(a) shows a comparison of the micro-crack shown in Figure 6(f) with the crater shown in Figure 6(m), while Figure 7(b) shows a comparison of the micro-crack shown in Figure 6(g) with the crater shown in Figure 6(n). The micro-cracks fit well with the contours of the craters and the positions of the nodule defects fit well with the positions of the nanoscale pinpoints, suggesting that the craters may be associated with nodule seeds that are tens of nanometers in diameter. As will be shown later based on FEM simulations, nodule seeds with diameters of tens of nanometers are absorption impurity defects.

Typical morphological features show that the laser-induced damage of the PLBS coatings is closely related to the following defects, including absorption defects at the
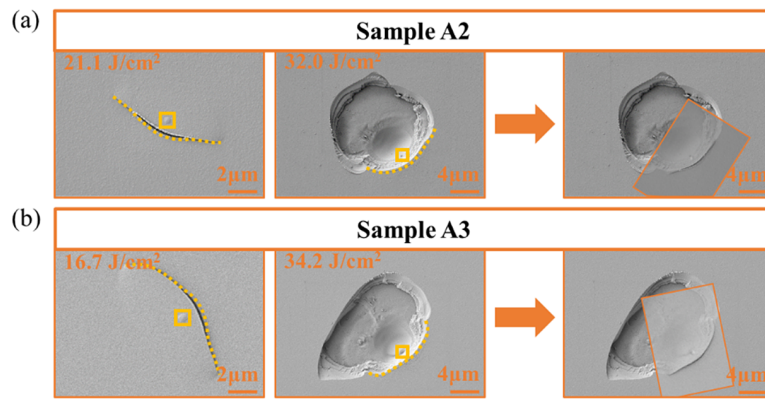
Figure 7. Comparison of micro-crack and crater-type morphologies.

Table 3. Thermal and optical parameters of materials used in the simulation.

Material	Density (g/cm^3)	Conductivity (W/(m·K))	Heat capacity (J/(K·g))	Refractive index	Extinction coefficient
BK7	2.51[33]	1.10[33]	0.858[33]	1.505	0
SiO$_2$	2.20[34]	1.00[34]	0.750[34]	1.414	0
HfO$_2$[34]	9.50	2.00	0.270	/	/
Al$_2$O$_3$	3.98[5]	1.60[35]	0.777[5]	1.585[18]	0
HfO$_2$–Al$_2$O$_3$	5.56	1.71	0.632	1.669	1.82×10^{-6}
HfO$_x$	9.50	2.00	0.270	2.000[36]	0.07[36]
CeO$_2$[7]	7.60	2.00	0.369	2.000	0.20

substrate–coating and layer–layer interfaces, and impurity particles on the substrate surface or in the coating (the seed of nodule defects). The impurity particles include subsurface impurities accumulated during the heating or material particles sputtered during deposition, etc. The particle density resulting from material sputtering is similar in the four PLBS coatings, and other types of defects are the main factors responsible for the differences in the LIDT.

To understand the mechanism of laser-induced damage of the PLBS coatings, the temperature rise caused by absorption defects and the E-field enhancement caused by nodule defects under laser irradiation are analyzed using FEM simulations. The simulation results for the area near the defect are presented below. The heat sources under laser irradiation include absorption defects and coatings. In practice, the composition and shape of the defects are extremely complex. For the simulations in this study, impurity defects (absorption nanoscale defects and nodule seeds) are simplified into spheres of a single material for qualitative analysis. For the laser-induced temperature-rise simulation, cases with absorption CeO$_2$ impurity defects or non-absorption Al$_2$O$_3$ impurity defects at the substrate–coating interface and nonstoichiometric HfO$_x$ defects at the layer–layer interface are analyzed. The parameters of the CeO$_2$, Al$_2$O$_3$ and HfO$_x$ defects are listed in Table 3. The parameters of the HfO$_2$–Al$_2$O$_3$ mixture layer, including its density, conductivity and heat capacity, are calculated from the parameters of HfO$_2$ and Al$_2$O$_3$ bulk materials based on the mixture ratio (HfO$_2$:Al$_2$O$_3$ = 0.4:1). The extinction coefficient (k) of the HfO$_2$–Al$_2$O$_3$ mixture layer is calculated

using Equation (2)[20] according to the data of coating A1, ignoring the absorption of the SiO$_2$ layer ($k = 0$):

$$1 + A/T = \exp\left(4\pi k d / \lambda\right). \tag{2}$$

Here, A is the measured absorption (9.2×10^{-6}), λ is the wavelength of interest (1064 nm), T is the transmittance at the wavelength of interest (81.3%) and d is the thickness of the coating, where only the thickness of the HfO$_2$–Al$_2$O$_3$ mixture layer (527.6 nm) is considered here. The calculated value of k is approximately 1.82×10^{-6}.

Firstly, assuming the presence of a HfO$_x$ particle at the interface between the fifth and sixth layers, we compare the effect of the CeO$_2$ particle density at the substrate–coating interface on the laser-induced temperature rise. The diameters of both HfO$_x$ and CeO$_2$ particles are set as 10 nm. As shown in Figure 8(a), the HfO$_x$ particle at the layer–layer interface results in a localized laser-induced temperature-rise distribution. As shown in Figure 8(b), when the CeO$_2$ particles are uniformly distributed at the substrate–coating interface at 7 μm intervals, a localized temperature rise is observed around the HfO$_x$ and CeO$_2$ particles, and the temperature around the CeO$_2$ particles is higher. As shown in Figure 8(c), when the density of the CeO$_2$ particles at the substrate–coating interface increases by five times, the laser-induced temperature rise increases significantly, and the highest temperature is recorded near the HfO$_x$ particle, which is approximately 1.9 times higher than that without CeO$_2$ particles at the substrate–coating interface. The simulation results show that the density of absorption defects on the
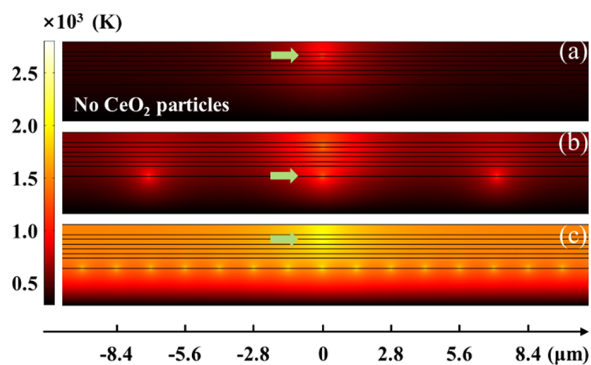
Figure 8. Simulated laser-induced temperature rise caused by (a) a HfO_x particle, (b) a HfO_x particle and CeO_2 particles at 7 μm intervals, and (c) a HfO_x particle and CeO_2 particles at 1.4 μm intervals.
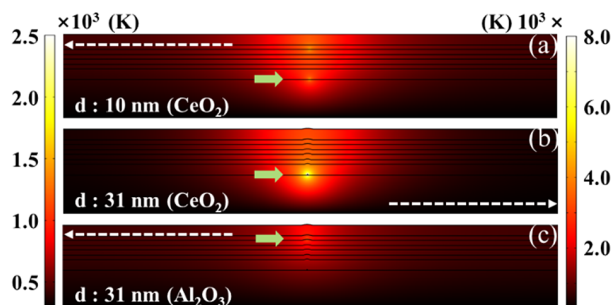

Figure 9. Simulated laser-induced temperature rise caused by a HfO_x particle and (a) a 10-nm-diameter CeO_2 particle, (b) a 31-nm-diameter CeO_2 particle and (c) a 31-nm-diameter Al_2O_3 particle.

substrate surface affects the laser-induced temperature-rise distribution, which consequently affects the LIDT and laser damage morphology of the coating[37]. This explains the difference in the depth of the initial damage morphology among the four PLBS coatings.

Then, still assuming the presence of a HfO_x particle at the interface between the fifth and sixth layers, we investigate the effects of different CeO_2 particle diameters and different particles (CeO_2 and Al_2O_3) on the laser-induced temperature-rise distribution. As shown in Figures 9(a) and 9(b), the CeO_2 particle diameter is set to 10 and 31 nm, the latter corresponding to the nodule seed diameter in Figure 6(f). Particles of this diameter can serve as seeds

to form nodules in the coating, as shown in Figure 9. As the CeO_2 particle diameter increases from 10 to 31 nm, the maximum temperature around the CeO_2 particle increases by approximately 5.4 times. While the temperature is not enhanced significantly by the non-absorption Al_2O_3 particle, the maximum laser-induced temperature rise occurs around the HfO_x particle, as shown in Figure 9(c).

Furthermore, the effects of different CeO_2 particle diameters and different particles (CeO_2 and Al_2O_3) on the E-field distribution are investigated. As shown in Figures 10(a) and 10(b), the CeO_2 particle diameter is set to 31 and 183 nm, the latter corresponding to the seed diameter in Figure 6(e). For the 31-nm-diameter CeO_2 seed, the E-field distribution in the PLBS coating is not enhanced significantly. As the CeO_2 seed diameter increases to 183 nm, local E-field enhancement around the nodule is observed, which primarily concentrated on the SiO_2 overcoat layer and mixture-on-SiO_2 interfaces. A comparison between Figures 10(b) and 10(c) shows no significant difference in the E-field distribution of the coatings induced by CeO_2 and Al_2O_3 seeds at an incident angle of 45°.

The simulation results indicate that for absorption particles with a diameter of approximately 30 nm, a significant temperature rise and thus high thermal stress will occur under laser irradiation. High thermal stress may contribute to the morphological feature of the micro-crack around nodule[30]. With increasing seed diameter, nodule defects will induce significant local E-field enhancement, thus resulting in a nodule-ejection damage morphology[38].

Experimental results indicate that there is a trade-off between the degree of oxidation of the coating and the migration and aggregation of subsurface impurities. Lowering the deposition temperature of the first layer adjacent to the substrate can suppress the migration and aggregation of subsurface impurities, thus improving the LIDT of the PLBS coating. However, if the deposition temperature is too low, it may lead to an increase in the sub-stoichiometry of the layer, thereby reducing the LIDT of the PLBS coating. In addition, as the deposition temperature of the subsequent layers increases, subsurface impurities will continue to migrate and accumulate. Therefore, under the conditions of a lower deposition temperature and fully oxidized coating, the
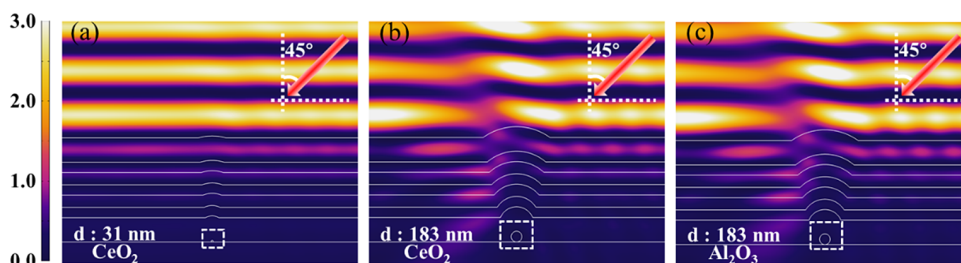

Figure 10. Simulated E-field distribution caused by (a) a 31-nm-diameter CeO_2 nodule seed, (b) a 183-nm-diameter CeO_2 nodule seed and (c) a 183-nm-diameter Al_2O_3 nodule seed.

absorption defect density at the substrate–coating interface is lower, and the LIDT of the coating is higher.

4. Conclusion

Substrate heat treatment experiments show that the subsurface impurities of the substrate will migrate to the surface and aggregate into larger particles on the substrate surface during the heat treatment. The higher the heat treatment temperature, the larger the size of the aggregated particles and the higher their density. The experimental and simulation results of the PLBS coatings show that subsurface impurity defects aggregate on the substrate surface to form particles with sizes of several to hundreds of nanometers, which become the source of absorption defects or nodule defect seeds in the coating. Impurity particles with diameters of several nanometers on the substrate surface will result in a temperature rise under laser irradiation. When the particle size increases to tens of nanometers, it will become the seed of nodule defects, resulting in a higher temperature rise, a greater thermal stress and hence micro-crack damage. When the particle size is further increased to hundreds of nanometers, the nodule defects result in significant local E-field enhancement under laser irradiation, resulting in nodule-ejection damage. A trick to increasing the LIDT of PLBS coatings is to use lower deposition temperatures at which the coating can be fully oxidized. In this study, the LIDT of the PLBS coating deposited at 140°C reaches 26.2 J/cm^2, which is 6.7 times that of the PLBS coating deposited at 200°C. We believe that the study of the laser damage mechanism of PLBS coatings can benefit other coatings with partial or high transmittance at laser wavelengths.

Acknowledgements

References

1. J. Zhu, J. Zhu, X. Li, B. Zhu, W. Ma, X. Lu, W. Fan, Z. Liu, S. Zhou, G. Xu, G. Zhang, X. Xie, L. Yang, J. Wang, X. Ouyang, L. Wang, D. Li, P. Yang, Q. Fan, M. Sun, C. Liu, D. Liu, Y. Zhang, H. Tao, M. Sun, P. Zhu, B. Wang, Z. Jiao, L. Ren, D. Liu, X. Jiao, H. Huang, and Z. Lin, High Power Laser Sci. Eng. **6**, e55 (2018).
2. R. Betti and O. A. Hurricane, Nat. Phys. **12**, 435 (2016).
3. F. Chen, J. Sun, Q. Wang, H. Zhu, F. Zeng, Y. Han, C. Lu, and G. Liu, Chin. Opt. Lett. **20**, 071101 (2022).
4. Y. Chai, M. Zhu, K. Yi, W. Zhang, H. Wang, Z. Fang, Z. Bai, Y. Cui, and J. Shao, Opt. Lett. **40**, 3731 (2015).
5. Z. Yu, H. He, W. Sun, H. Qi, M. Yang, Q. Xiao, and M. Zhu, Opt. Lett. **38**, 4308 (2013).
6. J. Cheng, J. Wang, J. Hou, H. Wang, and L. Zhang, Appl. Sci. **7**, 838 (2017).
7. Y. Chai, M. Zhu, K. Yi, H. Qi, H. Wang, W. Sun, Z. Yu, Z. Bai, Y. Zhao, and J. Shao, Proc. SPIE **9237**, 92370P (2014).
8. M. Yang, Y. Zhao, H. Shan, K. Yi, and J. Shao, Chin. J. Lasers **39**, 0803004 (2012).
9. X. Gao, G. Feng, J. Han, N. Chen, C. Tang, and S. Zhou, Appl. Opt. **51**, 2463 (2012).
10. X. Gao, G. Feng, J. Han, and L. Zhai, Opt. Express **20**, 22095 (2012).
11. C. Cai, Y. Liu, X. He, H. Zhao, G. Wang, J. Huang, Q. Hu, L. Xie, P. Ma, D. Yan, and L. Yin, Thin Solid Films **735**, 138876 (2021).
12. Z. Wang, L. Wang, W. Peng, Y. Cao, J. Yang, L. Tang and S. Li, Opt. Eng. **54**, 085102 (2015).
13. H. Liu, F. Wang, J. Huang, J. Meng, y. Ma, Y. Lian, L. Sun, X. Ye, F. Geng, X. Jiang, W. Wu, and L. Yang, Opt. Mater. **95**, 109231 (2019).
14. L. Sun, H. Liu, J. Huang, X. Ye, H. Xia, Q. Li, X. Jiang, W. Wu, L. Yang, and W. Zheng, Opt. Express **24**, 199 (2016).
15. Z. Zhao, J. Sun, M. Zhu, T. Zeng, C. Yin, K. Yi, Y. Zhao, Y. Cui, and J. Shao, Opt. Mater. **113**, 110890 (2021).
16. H. Qi, M. Zhu, M. Fang, S. Shao, C. Wei, K. Yi, and J. Shao, High Power Laser Sci. Eng. **1**, 36 (2013).
17. H. Liu, X. Ye, X. Zhou, J. Huang, F. Wang, X. Zhou, W. Wu, X. Jiang, Z. Sui, and W. Zheng, Opt. Mater. **36**, 855 (2014).
18. W. Du, M. Zhu, J. Shi, T. Liu, T. Zeng, J. Sun, K. Yi, and J. Shao, Opt. Laser Technol. **155**, 108399 (2022).
19. N. Xu, M. Zhu, J. Sun, Y. Chai, K. Yi, Y. Zhao, and J. Shao, Opt. Eng. **57**, 025101 (2018).
20. T. Zeng, M. Zhu, Y. Chai, J. Li, and J. Shao, Photonics Res. **9**, 229 (2021).
21. G. G. Stoney, Proc. R. Soc. London A **82**, 172 (1909).
22. W. Liu, C. Wei, J. Wu, Z. Yu, H. Cui, K. Yi, and J. Shao, Opt. Express **21**, 22476 (2013).
23. S. Fan, H. He, J. Shao, Z. Fan, and D. Zhang, Proc. SPIE **5774**, 531 (2004).
24. J. Shao, L. Sun, H. Liu, J. Huang, X. Ye, Q. Cheng, X. Zhou, F. Wang, X. Jiang, W. Wu, T. Jitsuno and W. Rudolph, Proc. SPIE **8786**, 87860P (2013).
25. Y. Pu, P. Kong, P. Ma, L. Lv, Q. Zhou, M. Zhang, Z. Lu, Z. Qiao, J. Die, and F. Qiu, Opt. Laser Technol. **151**, 108074 (2022).
26. J. Shi, M. Zhu, W. Du, T. Liu, L. Zhou, Y. Jiang, and J. Shao, Appl. Surf. Sci. **579**, 152192 (2022).
27. Q. Zhou, P. Ma, F. Qiu, Y. Pu, Z. Qiao, L. Lv, M. Zhang, P. Kong, R. Qiu, and Y. Jiang, Thin Solid Films **739**, 138963 (2021).
28. P. Post, L. Wurlitzer, W. Maus-Friedrichs, and A. P. Weber, Nanomaterials **8**, 530 (2018).
29. M. Zhu, H. Xing, Y. Chai, K. Yi, J. Sun, J. Wang, and J. Shao, Opt. Eng. **56**, 011003 (2017).
30. Y. Shan, H. He, C. Wei, Y. Wang, and Y. A. Zhao, Chin. Opt. Lett. **9**, 103101 (2011).
31. X. Cheng, A. Tuniyazi, J. Zhang, T. Ding, H. Jiao, B. Ma, Z. Wei, H. Li, and Z. Wang, Appl. Opt. **53**, A62 (2014).
32. X. Cheng, J. Zhang, T. Ding, Z. Wei, H. Li, and Z. Wang, Light. Sci. Appl. **2**, e80 (2013).

33. L. Su, Y. Chen, A. Y. Yi, K. Fritz, and P. Guido, Appl. Opt. **47**, 1662 (2008).
34. A. A. Kozlov, J. C. Lambropoulos, J. B. Oliver, B. N. Hoffman, and S. G. Demos, Sci. Rep. **9**, 607 (2019).
35. M. C. Wingert, J. Zheng, S. Kwon, and R. Chen, Semicond. Sci. Technol. **31**, 113003 (2016).
36. L. Gallais, J. Capoulade, J. Natoli, and M. Commandre, J. Appl. Phys. **104**, 053120 (2008).
37. M. Yang, Y. Zhao, H. Su, H. Shan, K. Yi, and J. Shao, Chin. J. Lasers **39**, 0807001 (2012).
38. T. Liu, M. Zhu, W. Du, J. Shi, J. Sun, Y. Chai, and J. Shao, High Power Laser Sci. Eng. **10**, e30 (2022).